日本磁気学会
ISSN 2432-0250
Journal of the Magnetics Society of Japan
Electronic Journal URL: https://www.jstage.jst.go.jp/browse/msjmag

Vol.49 No.4　2025

Journal

JOURNAL OF THE MAGNETICS SOCIETY OF JAPAN

Vol.49 No.4 2025

日本磁気学会

ISSN 2432-0250

HP: http://www.magnetics.jp/ e-mail: msj@bj.wakwak.com

Electronic Journal: http://www.jstage.jst.go.jp/browse/msjmag

TOEI

TPM-2-08s25

HcJの3σ/Ave. 0.2%※1を実現

渦電流補正方法※2も確立済

試料測定磁界
max 15Tesla

最大試料直径
10mm

パルス励磁型磁気特性測定装置

永久磁石および磁性体粉末を固形化した高磁化試料のヒステリシス曲線の自動測定および描画、SPD（Singuler Point Detection）測定が可能です。（RT～+200℃）

※1　電気学会資料 MAG-18-088 参照

※2　電気学会資料 MAG-07-011 参照

NdFeB(sintered) 測定例

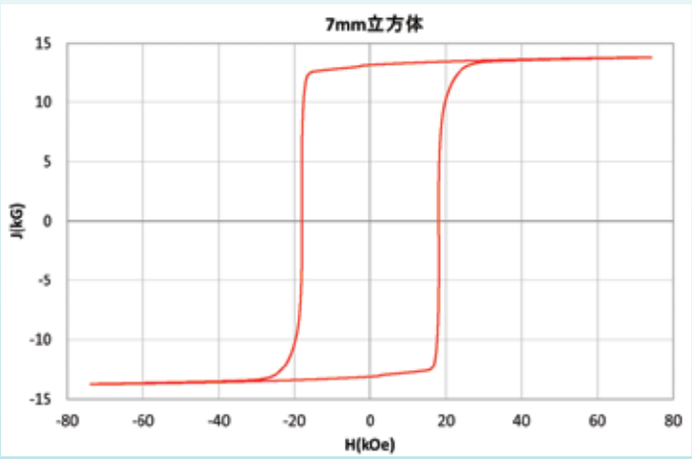

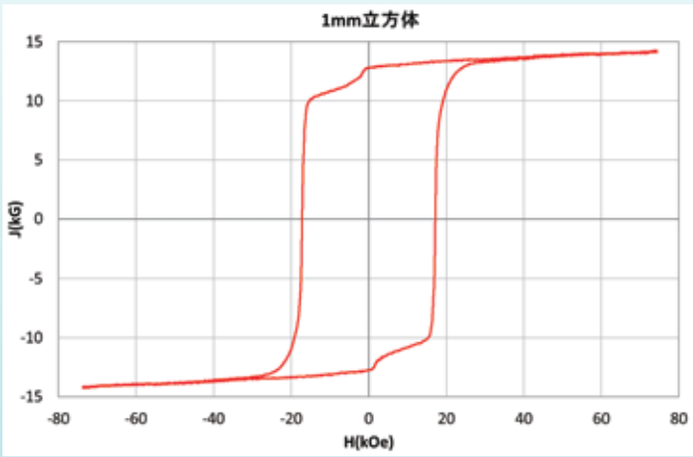

1mm 立方体測定用検出コイルはオプション品です

東英工業では他に振動試料型磁力計(VSM)、直流自記磁束計(JIS C2501 準拠)を始め、

各種磁気測定装置を取り揃えております。ぜひお問い合わせ下さい

TOEI 東英工業株式会社
http://www.toeikogyo.co.jp

〒194-0035 東京都町田市忠生1-8-13
TEL：042-791-1211 FAX：042-792-0490
E-mail：sales@toeikogyo.co.jp

Journal of the Magnetics Society of Japan
Vol. 49, No. 4

Electronic Journal URL: https://www.jstage.jst.go.jp/browse/msjmag

CONTENTS

J. Magn. Soc. Jpn., **49**, 47-57 (2025) <Paper>

Error Factors for Writability in Heat-Assisted Magnetic Recording

T. Kobayashi, I. Tagawa*, and Y. Nakatani**

Graduate School of Engineering, Mie Univ., *1577 Kurimamachiya-cho, Tsu 514-8507, Japan*

*Electrical and Electronic Engineering, Tohoku Institute of Technology, *35-1 Yagiyama-Kasumicho, Sendai 982-8577, Japan*

**Graduate School of Informatics and Engineering, Univ. of Electro-Communications, *1-5-1 Chofugaoka, Chofu 182-8585, Japan*

We analyze the error factors, namely erasure-before-write (EBW), erasure-after-write (EAW), Curie temperature T_c variation, write-error (WE), statistical factor, and anisotropy constant, for writability in heat-assisted magnetic recording (HAMR) employing a stochastic calculation. We separate the bit error rate bER for each grain column in 2 bits of data. We focus on the mean magnetization reversal numbers per unit time N_- and N_+ for the magnetization reversal in the recording direction and in the opposite direction to the recording direction, respectively, and the medium writing time τ_{med}, which is a time where the N_- value is large during writing. EBW and EAW are related to the T_c variation through the N_- value. WE can be improved by increasing the N_- and τ_{med} values and reducing the N_+ value. The increase in the grain number per bit is advantageous for reducing the bER value in terms of the statistical factor. The τ_{med} value is increased and the N_+ value is reduced by reducing the anisotropy constant. However, EAW increases due to the long τ_{med} value. Since the influence of EAW is large in HAMR, we may not reduce the anisotropy constant in HAMR as is possible in heated-dot magnetic recording.

Key words: HAMR, stochastic calculation, erasure-before-write, erasure-after-write, Curie temperature variation, write-error, statistical factor, anisotropy constant

1. Introduction

Heat-assisted magnetic recording (HAMR) is a promising candidate as a next generation magnetic recording method that can operate beyond the trilemma limit[1]. HAMR is a recording method where the medium is heated to reduce anisotropy during the writing period. There are many error factors that can affect writability in HAMR media.

Zhu and Li pointed out erasure-after-write (EAW)[2] as an error factor employing micromagnetic simulation. EAW means that when the writing field magnitude is too large, some grain magnetizations are reversed in the opposite direction to the recording direction caused by changing the writing field direction after writing.

Li and Zhu also discussed the impact of Curie temperature variation[3] on writability employing micromagnetic simulation.

Akagi *et al.* reported writability in heated-dot magnetic recording (HDMR), namely HAMR on bit patterned media, employing micromagnetic simulation. They assumed the medium material to be FePt. However, the anisotropy constant K_u was smaller[4] than that of bulk FePt.

We have discussed the influence of K_u on writability in HDMR employing a stochastic calculation based on the Néel-Arrhenius model with a Stoner-Wohlfarth dot. We explained why HDMR with a small K_u exhibits good writability using the mean magnetization reversal number per unit time in our stochastic calculation[5].

Corresponding author: T. Kobayashi (e-mail: kobayasi @phen.mie-u.ac.jp).

A feature of our stochastic calculation is that it is easy to grasp the physical implication of HAMR writing including HDMR.

In this paper, we analyze the effect of error factors, namely erasure-before-write, erasure-after-write, Curie temperature variation, write-error, statistical factor, and anisotropy constant, on writability in 4 Tbpsi shingled HAMR using the mean magnetization reversal number per unit time. We have already analyzed the error factors using ordinary write-error (WE) and EAW[2]. Previous WE included erasure-before-write (EBW). Here, we consider WE and EBW separately. We confirm the stochastic calculation result by employing a micromagnetic simulation.

2. Calculation Conditions and Method

2.1 Grain arrangement and medium structure

The grain arrangement and medium structure in 4 Tbpsi shingled HAMR are shown in Fig. 1. We chose a mean grain size D_m of 4.2 nm, a mean grain spacing Δ_G of 1.0 nm, a grain arrangement of 3 (row i) × 2 (column j) = 6 grains/bit. The grain height h was 8.5 nm, taking account of 10 years of archiving and adjacent track interference (ATI) as described in section 2.3. The bit length D_B and track width D_T were 10.4 and 15.6 nm, respectively. The x, y, and z directions were the down-track, cross-track, and film normal, respectively. The 3rd row (i = 3) grains were used as a guard band and the net grain number was 2×2 = 4 grains/bit.

We generated each grain size D_{ij} so that it had a log-normal distribution with a standard deviation σ_D. We used a σ_D/D_m value of 15 %.

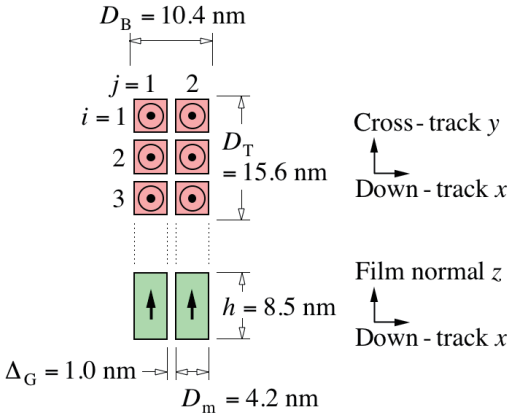

Fig. 1 Grain arrangement and medium structure in 4 Tbpsi shingled HAMR.

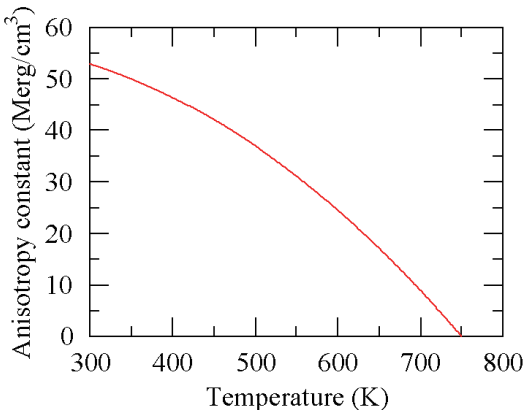

Fig. 2 Temperature dependence of anisotropy constant K_u.

2.2 Magnetic properties

The temperature T dependence of the medium magnetization M_s was calculated by employing mean field analysis[6] for $(Fe_{0.5}Pt_{0.5})_{1-c}Cu_c$, and that of the K_u value was assumed to be proportional to M_s^2[7]. $M_s(T_c = 770\ K, T = 300\ K) = 1000$ emu /cm^3 was assumed for FePt. Based on this assumption, the M_s value can be calculated for all values of T_c and T.

We used a mean Curie temperature T_{cm} of 750 K and a standard deviation σ_{Tc} of 2 %. The T_c distribution was assumed to be normal. Since each grain has a different T_c, the T_c value of each grain was adjusted by changing the Cu composition c for $(Fe_{0.5}Pt_{0.5})_{1-c}Cu_c$. We used a K_u value of 51 Merg/cm^3 and an anisotropy field H_k of 107 kOe at a readout temperature of 330 K. The temperature dependence of K_u is shown in Fig. 2.

2.3 Temperature profile and writing field

For the sake of simplicity, we used a thermal gradient $\partial T/\partial x$ of 12 K/nm in the down-track direction and assumed it to be constant anywhere when we calculated the writing field $|H_w|$ dependence of the bit error rate bER. A constant thermal gradient $\partial T/\partial y$ of 12 K/nm in the cross-track direction was also used for ATI. We also assumed the H_w value to be spatially uniform, the direction to be perpendicular to the medium plane, and the rise time to be zero.

Table 1 Standard calculation conditions.

Recording density (Tbpsi)	4
Mean grain size D_m (nm)	4.2
Standard deviation σ_D / D_m (%)	15
Mean grain spacing Δ_G (nm)	1.0
Grain height h (nm)	8.5
Bit length D_B (nm)	10.4
Track width D_T (nm)	15.6
Mean Curie temperature T_{cm} (K)	750
Standard deviation σ_{Tc} / T_{cm} (%)	2
Anisotropy constant K_u (330 K) (Merg / cm^3)	51
Anisotropy field H_k (330 K) (Oe)	107
Thermal gradient $\partial T / \partial x$ (K / nm)	12
Linear velocity v (m / s)	10
Gilbert damping constant α	0.1
Storage temperature (K) for 10 years of archiving	350
Thermal gradient $\partial T / \partial y$ (K / nm) for ATI	12
Exposure field (kOe) for ATI	10
Exposure time (ns) for ATI	1

The standard calculation conditions are summarized in Table 1. The linear velocity v was 10 m/s. The Gilbert damping constant α was 0.1. When we choose an h value, 10 years of archiving, ATI, and writability must be dealt with simultaneously, since they are in a trade-off relationship. We assumed the storage temperature to be 350 K for 10 years of archiving, for which we took a certain margin into account. The maximum temperature of the grains at the edge of the writing track was assumed to be $T_{cm} + 2\sigma_{Tc}$ for ATI. Based on this assumption, almost all grains in the writing track are heated to above their Curie temperatures during the writing period. The 3rd row (i = 3) grains were used as a guard band as described in section 2.1. The temperatures of the 1st and 2nd row (i = 1 and 2) grains at the adjacent track were $T_{cm} + 2\sigma_{Tc} - (4 - i)(D_m + \Delta_G)\partial T/\partial y$ = 593 and 655 K, respectively. We used an exposure field of 10 kOe and a time of 1 ns for ATI. We fixed the h value at 8.5 nm[8], taking account of 10 years of archiving and ATI. The limiting factor was ATI. The grain aspect ratio h/D_m was 2.0.

2.4 Stochastic calculation method

The information stability for 10 years of archiving has been discussed employing the Néel-Arrhenius model with a Stoner-Wohlfarth grain[1]. During writing in HAMR, the magnetization reversal is the non-Néel-Arrhenius type where $|H_w| > H_k$. However, the duration for the non-Néel-Arrhenius type is very short, and most of the writing time is the Néel-Arrhenius type where $|H_w| < H_k$. Therefore, stochastic magnetization reversal

under thermal agitation is dominant even as regards writability.

The mean magnetization reversal number per unit time N is expressed as

$$N = f_\alpha \exp(-K_\beta), \tag{1}$$

based on the Néel-Arrhenius model with a Stoner-Wohlfarth grain, where f_α is the attempt frequency[9] and K_β is the thermal stability factor. The f_α value gives an attempt number per unit time for magnetization reversal, and the Boltzmann factor $\exp(-K_\beta)$ is interpreted as the probability of magnetization reversal.

When the $|H_w|$ value is less than H_k, $f_\alpha \equiv f_{\alpha+}$, $K_\beta \equiv K_{\beta+}$, and $N \equiv N_+$ are given by

$$f_{\alpha+} = \frac{\gamma\alpha}{1+\alpha^2}\sqrt{\frac{M_s H_k^3 V}{2\pi kT}}\left(1-\left(\frac{|H_w|}{H_k}\right)^2\right)\left(1+\frac{|H_w|}{H_k}\right), \tag{2}$$

$$K_{\beta+} = \frac{K_u V}{kT}\left(1+\frac{|H_w|}{H_k}\right)^2, \text{ and} \tag{3}$$

$$N_+ = f_{\alpha+}\exp(-K_{\beta+}), \tag{4}$$

respectively, for magnetization reversal in the opposite direction to the recording direction, where γ, α, V, and k are the gyromagnetic ratio, Gilbert damping constant, grain volume $V = D_{ij}^2 \times h$, and Boltzmann constant, respectively. We used a γ value of 1.76×10^7 rad s^{-1} Oe^{-1}. For magnetization reversal in the recording direction, $f_\alpha \equiv f_{\alpha-}$, $K_\beta \equiv K_{\beta-}$, and $N \equiv N_-$ are given by

$$f_{\alpha-} = \frac{\gamma\alpha}{1+\alpha^2}\sqrt{\frac{M_s H_k^3 V}{2\pi kT}}\left(1-\left(\frac{|H_w|}{H_k}\right)^2\right)\left(1-\frac{|H_w|}{H_k}\right), \tag{5}$$

$$K_{\beta-} = \frac{K_u V}{kT}\left(1-\frac{|H_w|}{H_k}\right)^2, \text{ and} \tag{6}$$

$$N_- = f_{\alpha-}\exp(-K_{\beta-}), \tag{7}$$

respectively.

In our stochastic calculation, we used the effective anisotropy constant K_{ueff} instead of K_u and the effective anisotropy field H_{keff} instead of H_k, taking account of the shape anisotropy[10], as

$$K_{ueff} = K_u + \frac{(4\pi-3N_z)M_s^2}{4}, \tag{8}$$

$$N_z = 8\arctan\left(\frac{D_x D_y}{h\sqrt{D_x^2+D_y^2+h^2}}\right), \text{ and} \tag{9}$$

$$H_{keff} = \frac{2K_{ueff}}{M_s}. \tag{10}$$

The magnetostatic field from surrounding grains was ignored.

Although there is a period during writing where $|H_w| > H_{keff}$, the duration is relatively short. The factor $\sqrt{M_s H_k^3/T}$ in Eqs. (2) and (5) has a strong impact on the temperature dependence of $f_{\alpha\pm}$, and $(1-(|H_w|/H_k)^2)(1\pm|H_w|/H_k)$ is a weakly impacting factor since the H_k value is considerably larger than $|H_w|$ for most of the writing time. Although the $\sqrt{M_s H_k^3/T}$ value becomes zero at T_c, $(1-(|H_w|/H_k)^2)(1\pm|H_w|/H_k)$ reaches zero at a temperature where $H_k = |H_w|$. We employed the Néel-Arrhenius model for the entire writing time. To achieve this, we extended the $f_{\alpha\pm}$ formula to T_c as follows

$$f_{\alpha\pm} = \frac{\gamma\alpha}{1+\alpha^2}\sqrt{\frac{M_s H_{keff}^3 V}{2\pi kT}}\left(1-\left(\frac{|H_w|}{H_{const}}\right)^2\right)\left(1\pm\frac{|H_w|}{H_{const}}\right), \tag{11}$$

so that the $f_{\alpha\pm}$ value become zero at T_c. H_{const} in Eq. (11) is a fitting parameter for Eqs. (2) and (5) and we used a H_{const} value of 60 kOe. When $|H_w| > H_{keff}$, we assumed that

$$\exp(-K_{\beta-}) = 1. \tag{12}$$

The calculation procedure for the $|H_w|$ dependence of bER, namely writability, is described below. The dot temperature fell with time from T_c according to $\partial T/\partial x$ and v. The attempt times were calculated using $f_{\alpha\pm}$. The probabilities $\exp(-K_{\beta\pm})$ were calculated for every attempt time. The magnetization direction was determined by the Monte Carlo method for every attempt time. Then the bER value was obtained. The calculation detail has already been reported[11].

The bER value in this paper is useful only for comparison.

3. Calculation Results

3.1 Erasure-before-write and erasure-after-write

Figure 3 (a) shows the $|H_w|$ dependence of the bER for 1 bit ("010" data using $2\times2 = 4$ grains) and 2 bits of data ("0110" data using $2\times4 = 8$ grains). The readout signal to noise ratio depends on the bit length and reader resolution. However, our bER depends on the magnetization direction and area of grains[11]. Therefore, the bER for 1 bit of data is intrinsically larger than that for 2 bits of data.

2 bits of data consist of 8 grains and 1 column consists of 2 grains. We calculated the bER value using 2 of the 8 grains for each column in 2 bits of data. Figure 3 (b) shows the $|H_w|$ value dependence of the 2 grain bER value for a column number j of 1 to 4.

We calculated the mean magnetization reversal number per unit time $N_- = f_{\alpha-}\exp(-K_{\beta-})$ as a function of time during writing to analyze the result in Fig. 3, and the results are shown in Figs. 4, 5, and 6. The N_- value is for the magnetization reversal to the H_w direction from the antiparallel direction to the H_w direction. At a time of zero, the H_w direction changes from downward to upward. At a time of $(j-1)(D_m+\Delta)/v$, the grain temperature for j is T_{cm}. At a time of 2.07 ns, which is the field writing time, namely the writing time defined

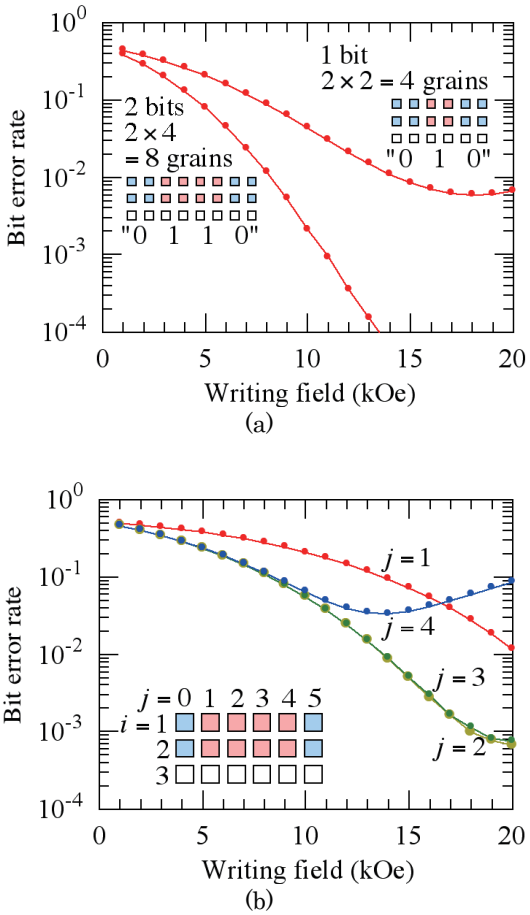

Fig. 3 (a) Writing field $|H_w|$ dependence of bit error rate bER for 1 bit ("010" data using $2 \times 2 = 4$ grains) and 2 bits of data ("0110" data using $2 \times 4 = 8$ grains) in 4 Tbpsi shingled HAMR. (b) $|H_w|$ dependence of bER value ($2 \times 1 = 2$ grains) for each column number $j = 1$ to 4.

by H_w, for 2 bits of data, the H_w direction changes from upward to downward. Figure 4 shows the result for $T_c = T_{cm} + \sigma_{Tc}$, T_{cm}, and $T_{cm} - \sigma_{Tc}$ where $j = 1$ and $|H_w| = 10$ kOe, Fig. 5 shows the result where $j = 4$ and $|H_w| = 20$ kOe, and Fig. 6 shows the result where $j = 2$ and $|H_w| = 20$ kOe. The grain temperature for $j = 1$ is also shown in Fig. 4. If there is a T_c variation, the time is advanced by $\tau_{Tc} = \sigma_{Tc}/((\partial T/\partial x) \cdot v)$ for a grain with $T_c = T_{cm} + \sigma_{Tc}$, and is delayed by τ_{Tc} for a grain with $T_c = T_{cm} - \sigma_{Tc}$.

As shown in Fig. 3 (b), the 2 grain bER value for $j = 1$ decreases as the $|H_w|$ value increases, and the bER value at $|H_w| = 10$ kOe is larger than those for other j values. When the temperature of a grain with $T_c = T_{cm}$ in $j = 1$ decreases to just T_c at a time of zero as shown in Fig. 4, the magnetization z component is in the recording direction with a probability of 50 % and in the opposite direction also with a probability of 50 % since the grain almost shows paramagnetism. The H_w direction changes from downward to upward at a time of zero, and the magnetization in the opposite direction reverses to the recording direction with a certain

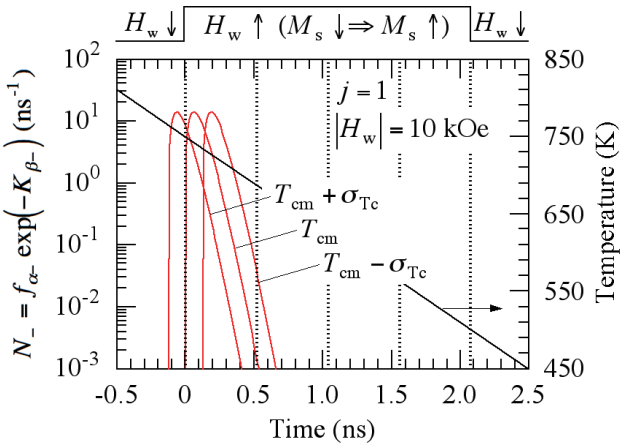

Fig. 4 Mean magnetization reversal number per unit time $N_- = f_{\alpha-} \exp(-K_{\beta-})$ as a function of time during writing for Curie temperatures of $T_{cm} + \sigma_{Tc}$, T_{cm}, and $T_{cm} - \sigma_{Tc}$ where $j = 1$ and $|H_w| = 10$ kOe. Grain temperature for $j = 1$ is also shown.

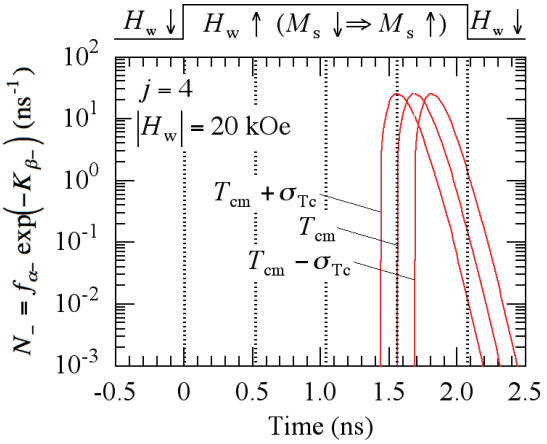

Fig. 5 Mean magnetization reversal number per unit time $N_- = f_{\alpha-} \exp(-K_{\beta-})$ as a function of time during writing for Curie temperatures of $T_{cm} + \sigma_{Tc}$, T_{cm}, and $T_{cm} - \sigma_{Tc}$ where $j = 4$ and $|H_w| = 20$ kOe.

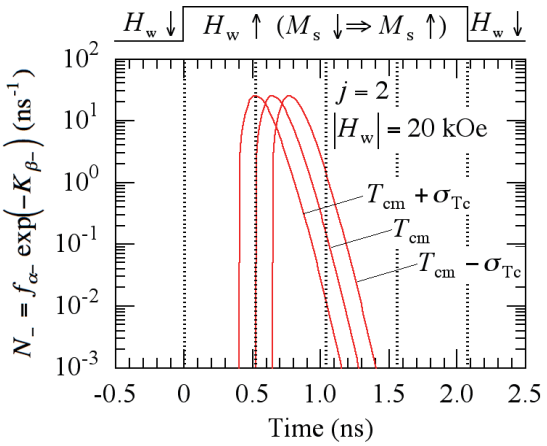

Fig. 6 Mean magnetization reversal number per unit time $N_- = f_{\alpha-} \exp(-K_{\beta-})$ as a function of time during writing for $j = 2$ where $|H_w| = 20$ kOe.

probability. However, the temperature of a grain with $T_c = T_{cm} + \sigma_{Tc}$ decreases to T_c at a time of $-\tau_{Tc}$. The H_w direction is downward between times of $-\tau_{Tc}$ and zero as shown in Fig. 4. Therefore, more than half of the grains are magnetized in the opposite direction to the recording direction at a time of zero. We call this erasure-before-write (EBW). The bER value is increased by EBW.

Next, we discuss the 2 grain bER value in $j = 4$. The bER value for $|H_w| > 10$ kOe is larger than that for $j = 2$ or 3 as shown in Fig. 3 (b). This is due to EAW[2)] as shown in Fig. 5. The magnetization reverses to the downward direction with a certain probability after a field writing time of 2.07 ns, at which the H_w direction changes to downward, before the grain temperature decreases and the magnetization direction is fixed. Since the N_- value increases as the $|H_w|$ value increases, EAW also increases as shown in Fig. 3 (b).

For $j = 2$, the 2 grain bER value is small as shown in Fig. 3 (b), since there is no EBW and no EAW as shown in Fig. 6. There is also no EBW and no EAW for $j = 3$. Therefore, the bER values are the same for $j = 2$ and 3 as shown in Fig. 3 (b).

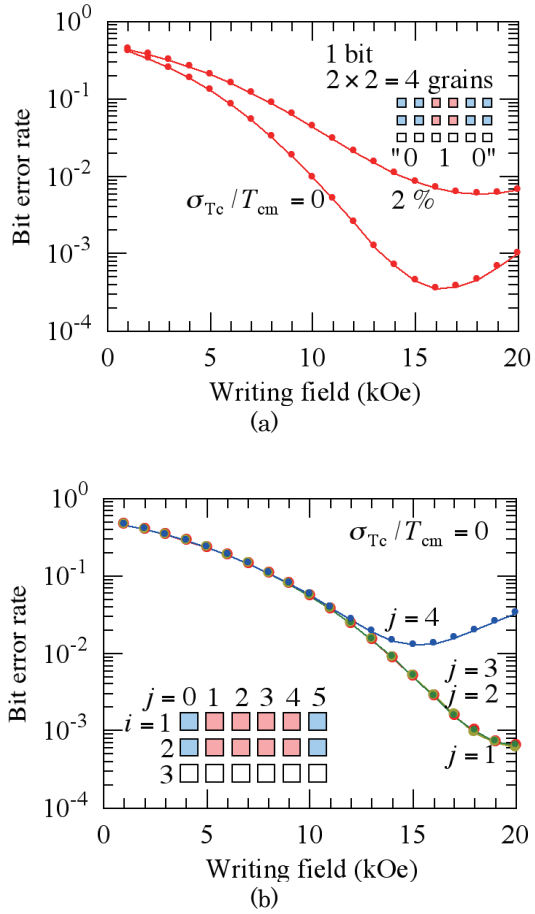

Fig. 7 (a) Writing field $|H_w|$ dependence of bit error rate bER for 1 bit of data where $\sigma_{Tc}/T_{cm} = 2$ and 0 %. (b) $|H_w|$ dependence of 2 grain bER value for each column number $j = 1$ to 4 where $\sigma_{Tc}/T_{cm} = 0$ %.

The bER for 1 bit of data corresponds to those for $j = 1$ and 4. Therefore, the bER value for 1 bit of data is intrinsically larger than that for 2 bits of data as shown in Fig. 3 (a).

3.2 Curie temperature variation

T_c variation is important for EBW and EAW. We compared the result for $\sigma_{Tc}/T_{cm} = 0$ % with that for 2 %. Figure 7 (a) shows the $|H_w|$ dependence of the bER for 1 bit of data. The bER values for $\sigma_{Tc}/T_{cm} = 2$ and 0 % were 4.4×10^{-2} and 1.0×10^{-2}, respectively, at $|H_w| = 10$ kOe. Figure 7 (b) shows the 2 grain bER value for $\sigma_{Tc}/T_{cm} = 0$ % in 2 bits of data. The bER values with and without T_c variation are the same for $j = 2$ or 3 as shown in Figs. 3 (b) and 7 (b), respectively, since there is no EBW and no EAW. When $\sigma_{Tc}/T_{cm} = 0$ %, the bER value for $j = 1$ is the same as that for $j = 2$ or 3, since there is no EBW. And the bER value for $j = 4$ is smaller than that for $j = 4$ in Fig. 3 (b), since there is no T_c variation.

One cause of EBW is T_c variation. However, EBW

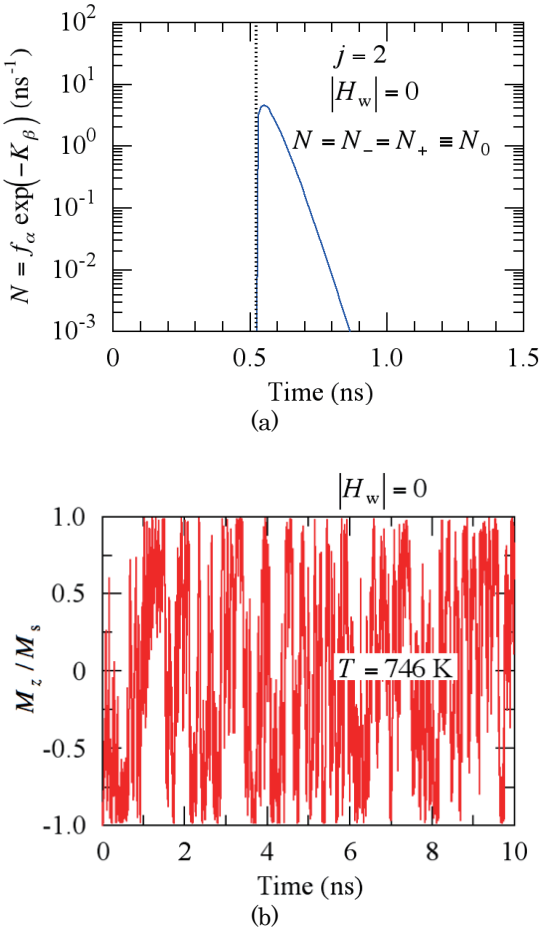

Fig. 8 (a) Mean magnetization reversal number per unit time $N = f_\alpha \exp(-K_\beta)$ as a function of time where $N_0 = 4.6$ ns^{-1} at 0.55 ns (746 K) and (b) time dependence of magnetization z component M_z/M_s at 746 K (0.55 ns) where $|H_w| = 0$ and $H_{keff} = 13$ kOe.

may also occur in granular media with no T_c variation, since the grain position fluctuates. And T_c variation makes EAW large.

3.3 Write-error

If there is no EBW and no EAW, the 2 grain bER value for j = 2 or 3 decreases as the $|H_w|$ value increases as shown in Fig. 3 (b), since WE decreases. WE can be explained using the mean magnetization reversal number per unit time N.

First, Fig. 8 (a) shows the $N = N_- = N_+ \equiv N_0$ value for $|H_w|$ = 0 as a function of time during writing for j = 2. The magnetization reversal numbers are the same in the recording direction and in the opposite direction to the recording direction, since the N_+ and N_- values are the same for $|H_w|$ = 0. The N_0 value exhibits its maximum value at 0.55 ns where the temperature is 746 K. We confirmed the meaning of N_0 in Fig. 8 (a) by employing a micromagnetic simulator, EXAMAG LLG (Fujitsu Ltd.)[12], in which the Landau-Lifshitz-Gilbert (LLG) equation is solved by the finite-element method. We added the equivalent field for the thermal agitation energy. The calculation step time was 10^{-16} s. We focused on the magnetization motion at 746 K where the time in Fig 8 (a) is 0.55 ns. Figure 8 (b) shows the time dependence of magnetization z component M_z/M_s, which was calculated by employing a micromagnetic simulation and that indicates the magnetization motion as a function of time. The initial magnetization direction is the $-z$ direction. The calculation temperature was constant at 746 K where H_{keff} = 13 kOe. Since N_0 = 4.6 ns^{-1} at 746 K, we can expect there to be 46 mean magnetization reversals within 10 ns. Although we cannot count the magnetization reversal number exactly from Fig. 8 (b), several dozen magnetization reversals can be seen.

Next, the N_0 ($|H_w|$ = 0), N_-, and N_+ values as a function of time when $|H_w|$ = 5 kOe are shown in Fig. 9 (a), where the N_+ value is the mean magnetization reversal number per unit time in the opposite direction

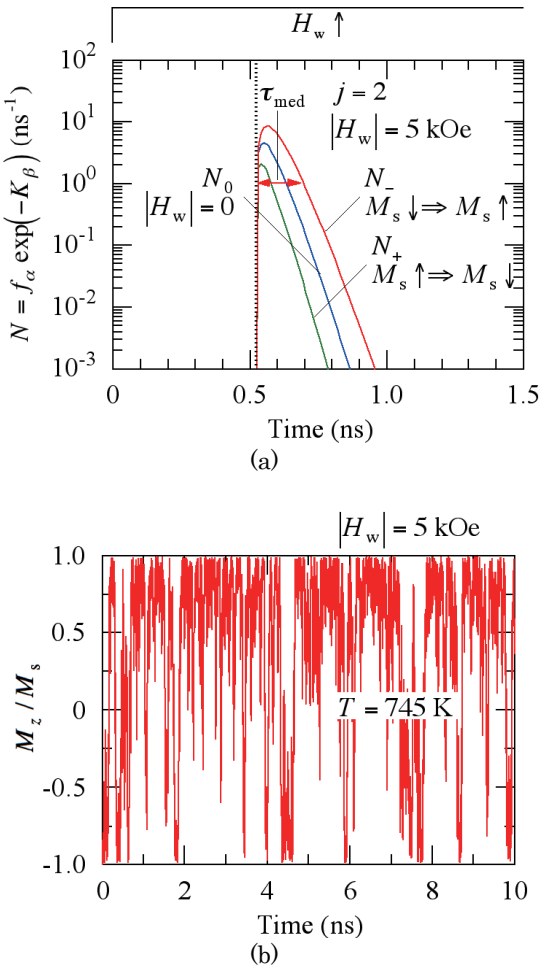

Fig. 9 (a) Mean magnetization reversal number per unit time $N = f_\alpha \exp(-K_\beta)$ as a function of time where N_- = 8.5 ns^{-1} and N_+ = 1.6 ns^{-1} at 0.56 ns (745 K) and (b) time dependence of magnetization z component M_z/M_s at 745 K (0.56 ns) where $|H_w|$ = 5 kOe and H_{keff} = 15 kOe.

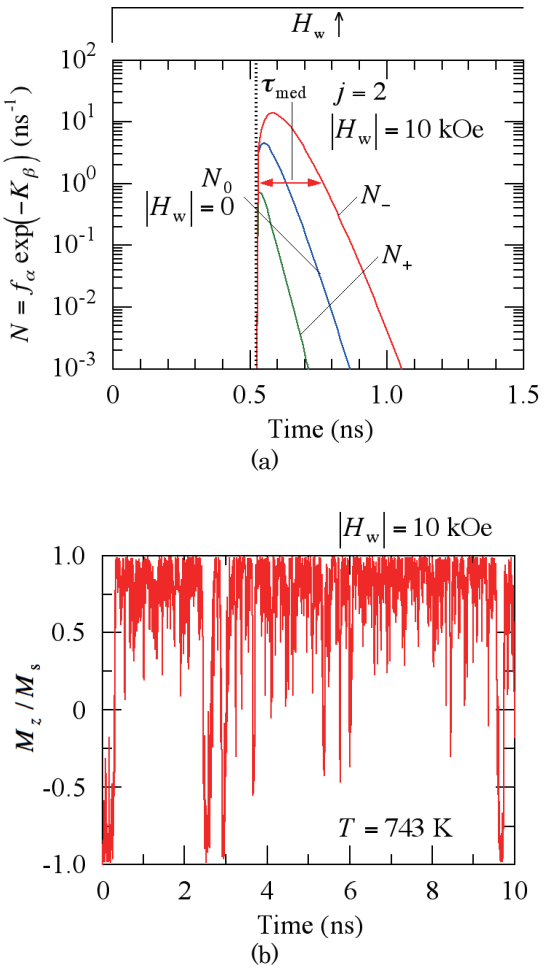

Fig. 10 (a) Mean magnetization reversal number per unit time $N = f_\alpha \exp(-K_\beta)$ as a function of time where N_- = 13.7 ns^{-1} and N_+ = 0.20 ns^{-1} at 0.58 ns (743 K) and (b) time dependence of magnetization z component M_z/M_s at 743 K (0.58 ns) where $|H_w|$ = 10 kOe and H_{keff} = 18 kOe.

to the recording direction. The N_- value is larger and the N_+ value is smaller than the N_0 value. We introduced a medium writing time τ_{med}, namely the writing time determined by medium where the N_- value is larger than 1 ns^{-1} as shown in Fig. 9 (a). A value of 1 ns^{-1} is tentative. Since the writing time has an order of 1 ns, we chose this value as a guideline. The τ_{med} value was 0.18 ns. On the other hand, the N_- value exhibits its maximum value of 8.5 ns^{-1} at 0.56 ns, which corresponds to a temperature of 745 K. The $1/N_-$ value represents the mean time between stochastically induced magnetization reversals under thermal agitation[13], and $1/N_- = 0.12$ ns. The τ_{med} value of 0.18 ns, which corresponds to the duration to write data in the medium, is comparable to $1/N_- = 0.12$ ns. This means that there is no margin for writing. Therefore, WE occurs. Figure 9 (b) shows the time dependence of M_z/M_s at 745 K where $|H_w| = 5$ kOe and $H_{keff} = 15$ kOe. The writing field direction is the z direction. Since $N_+ = 1.6$ ns^{-1} at 745 K, we can expect there to be 16 mean magnetization reversals within 10 ns in the $-z$ direction. If we employ a definition stating that the magnetization is reversed when the M_z/M_s value falls below -0.9, the magnetization reversal number is about 11 or 12 times for the example shown in Fig. 9 (b). It can be seen that the magnetization motion in the $-z$ direction is reduced compared with that in Fig. 8 (b).

When $|H_w| = 10$ kOe, N_- exhibits its maximum value of 13.7 ns^{-1} at 0.58 ns, which corresponds to a temperature of 743 K, as shown in Fig. 10 (a). The $1/N_-$ value was reduced to 0.073 ns and the τ_{med} value was increased to 0.25 ns compared with $1/N_- = 0.12$ ns and $\tau_{med} = 0.18$ ns for $|H_w| = 5$ kOe. Therefore, the writing margin increases and WE decreases. Figure 10 (b) shows the time dependence of M_z/M_s at 743 K where $|H_w| = 10$ kOe and $H_{keff} = 18$ kOe. Since $N_+ = 0.20$ ns^{-1}, we can expect there to be 2.0 mean magnetization reversals within 10 ns in the $-z$ direction. The magnetization reversal number is 3 times for the example shown in Fig. 10 (b). The magnetization motion in the $-z$ direction is further reduced compared with that in Fig. 9 (b).

Figure 11 is a schematic illustration of the magnetization motion during writing. At the initial time of writing, the magnetization direction is antiparallel (a1) or parallel (b1) to the H_w direction. There are many cases with respect to the magnetization motion. There is a small probability that the magnetization maintains its initial direction antiparallel (a1) to H_w until the end of writing. The magnetization direction changes from antiparallel to parallel (a2) with a large probability determined by N_-. After (a2), the magnetization direction reverses to antiparallel again (a3) with a very small probability determined by N_+. On the other hand, there are also many cases for an initial direction parallel to H_w where the magnetization maintains its direction (b1), changes to antiparallel (b2), and reverses to parallel again (b3). If the N_+ value is small, the opportunity for realizing (a3) or (b2) is small.

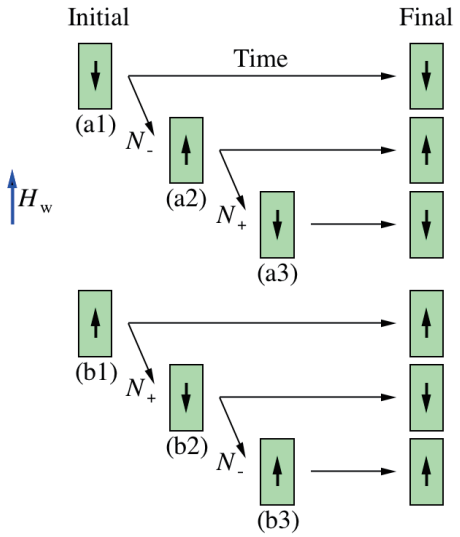

Fig. 11 Schematic illustration of magnetization motion during writing.

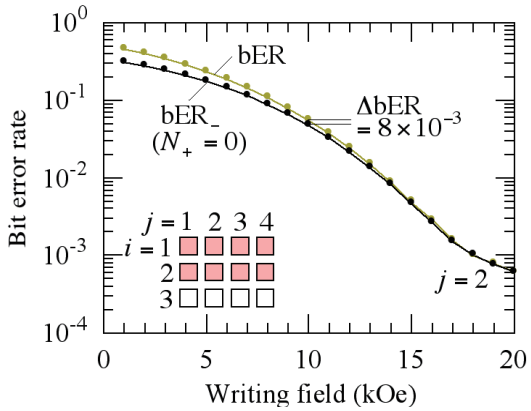

Fig. 12 Comparison of two cases of writing field $|H_w|$ dependence of 2 grain bER for column number $j = 2$. The bER value was calculated using both N_- and N_+, and the bER_ value was calculated using only N_- where $N_+ = 0$.

N_+ is a value that cannot be ignored. A comparison of two cases in the 2 grain bER for $j = 2$ is shown in Fig. 12, where the bER value was calculated using both N_- and N_+, and the bER_ value was calculated using only N_- where $N_+ = 0$. The bER_ value is smaller than the bER value, and the difference $\Delta bER = bER - bER_-$ becomes large as the $|H_w|$ value decreases. As shown in Fig. 9 (a), when the $|H_w|$ value is small, the difference between the N_- and N_+ values is small and the N_+ value is large. This means that there is a high probability of magnetization reversal in the opposite direction to the recording direction. The bER and bER_ values are 5.6×10^{-2} and 4.8×10^{-2}, respectively, and the ΔbER value is 8×10^{-3} at $|H_w| = 10$ kOe. When aiming for a bER of 10^{-3}, a value of 8×10^{-3} is large. Therefore, the N_+ value has a large influence on WE.

The $1/N_-$ value must be short and the τ_{med} value must be long to increase the probability of magnetization

reversal into the recording field direction. Moreover, the N_+ value must be small to reduce the magnetization reversal in the opposite direction to the recording direction. As seen in Figs. 9 (a) and 10 (a), the N_- and τ_{med} values increase and the N_+ value decreases as the $|H_w|$ value increases. As a result, WE decreases as the $|H_w|$ value increases as shown in Fig. 3 (b) for j = 2 or 3.

3.4 Statistical factor

The statistical factor means that the bER value decreases as the grain number increases. If one bit contains many grains, the bER value becomes low since the probability of a simultaneous error is very low for more than half of the grains in one bit.

The 4 grain bER value for j = 2 and 3 with no EBW and no EAW is smaller than the 2 grain bER value for j = 2 or 3 as shown in Fig. 13 due to the statistical factor. The 4 grain bER value in Fig. 3 (a) is larger than the 4 grain bER value in Fig. 13, since the 4 grain bER value in Fig. 3 (a) corresponds to those for j = 1 and 4. The bER value for 2 bits of data with 8 grains in Fig. 3 (a) is even smaller than the 4 grain bER value in Fig. 13.

The increase in the grain number per bit is advantageous for reducing the bER value in terms of the statistical factor. However, that is disadvantageous as regards manufacturability, since it is difficult to manufacture grains with a small D_m and a large h/D_m.

In short, the error factors for 2 bits of data in Fig. 3 (a) are erasure-before-write, T_c variation, and write-error for j = 1, write-error only for j = 2 or 3, and erasure-after-write, T_c variation, and write-error for j = 4. The bER value in 1 bit of data corresponds to those for j = 1 and 4. Furthermore, 2 bits of data with 8 grains is more advantageous than 1 bit of data with 4 grains thanks to the statistical factor. Therefore, the bER value for 1 bit of data is intrinsically larger than that for 2 bits of data as shown in Fig. 3 (a).

3.5 Anisotropy constant

It has been reported that writability can be improved by using a medium with a small anisotropy constant K_u in HDMR[4]. We have explained the reason using the N_- and N_+ values[5]. Therefore, we examined the effect of a small K_u on writability in HAMR. Given that 10 years of archiving and ATI are worse when we use a small K_u medium, the h value must be increased at the same time for practical use. However, here we discuss only the effect of a small K_u and fixed the h value at 8.5 nm. We used an anisotropy constant ratio K_u/K_{bulk}[11] instead of K_u in this section. The $K_u(T)$ value as shown in Fig. 2 corresponds to K_u/K_{bulk} = 0.8. When the T_c values are the same, the $K_u(T)$ values for K_u/K_{bulk} = 0.6 and 0.4 are three quarters and one half of the $K_u(T)$ value for K_u/K_{bulk} = 0.8, respectively, for all values of T.

Figure 14 (a) shows the $|H_w|$ value dependence of the bER value in 1 bit of data calculated employing our stochastic calculation for various K_u/K_{bulk} values. When $|H_w|$ = 5 kOe, the bER value decreases as the K_u/K_{bulk} value decreases, and when $|H_w|$ = 20 kOe, the bER value increases. The bER value around 10 kOe is important as regards practical use and the bER value appears to be at its minimum around K_u/K_{bulk} = 0.6 at 10 kOe. We also confirmed the result in Fig. 14 (a) by

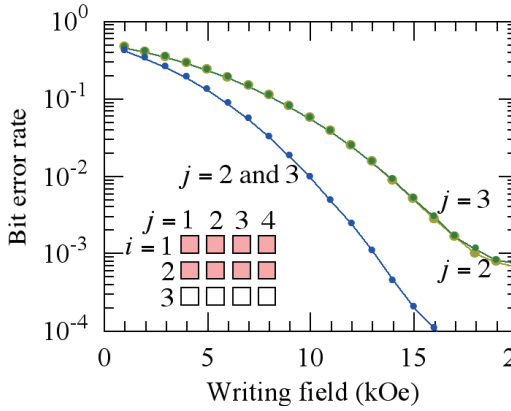

Fig. 13 Writing field $|H_w|$ dependence of bER for column number j = 2, 3 (2 grains), 2 and 3 (4 grains).

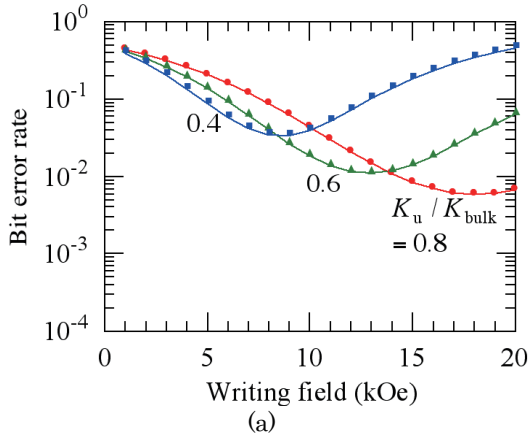

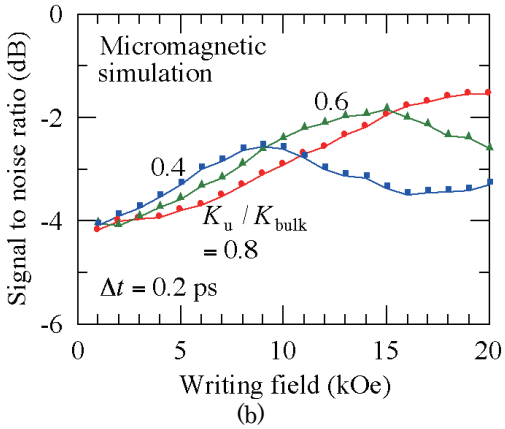

Fig. 14 Writing field $|H_w|$ dependence of (a) bit error rate bER for 1 bit of data calculated employing our stochastic calculation and (b) signal to noise ratio SNR calculated employing a micromagnetic simulation for various anisotropy constant ratios K_u/K_{bulk} where the calculation step time Δt = 0.2 ps.

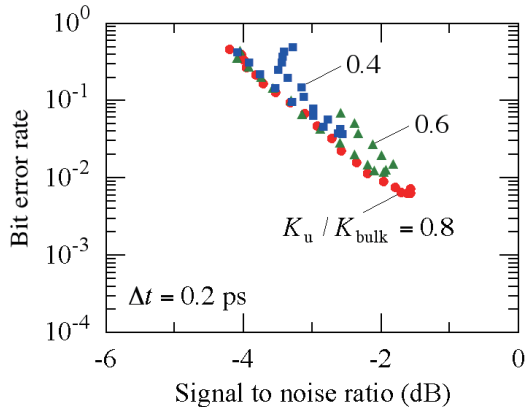

Fig. 15 The bER calculated employing our stochastic calculation as a function of SNR calculated employing a micromagnetic simulation.

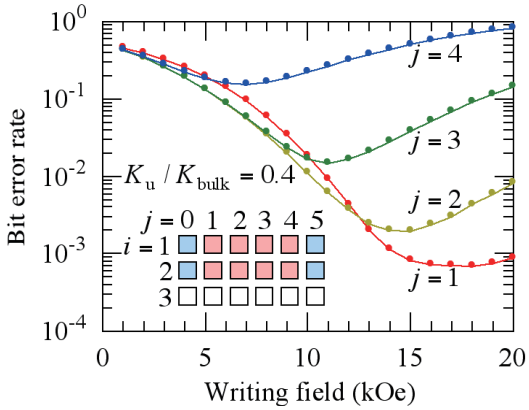

Fig. 16 Writing field $|H_w|$ dependence of 2 grain bER for each column number j = 1 to 4 where K_u/K_{bulk} = 0.4.

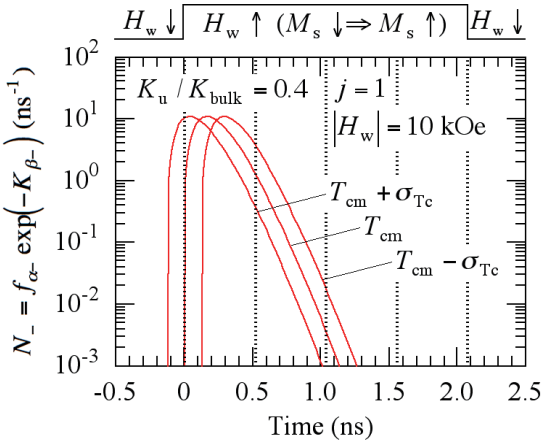

Fig. 17 Mean magnetization reversal number per unit time $N_- = f_{\alpha-} \exp(-K_{\beta-})$ as a function of time during writing for Curie temperatures of $T_{cm} + \sigma_{Tc}$, T_{cm}, and $T_{cm} - \sigma_{Tc}$ where K_u/K_{bulk} = 0.4, j = 1, and $|H_w|$ = 10 kOe.

employing a micromagnetic simulation in which we solved the LLG equation. The LLG calculation method has already been reported in detail[8]. Figure 14 (b) shows the $|H_w|$ value dependence of the signal to noise ratio SNR calculated employing a micromagnetic simulation

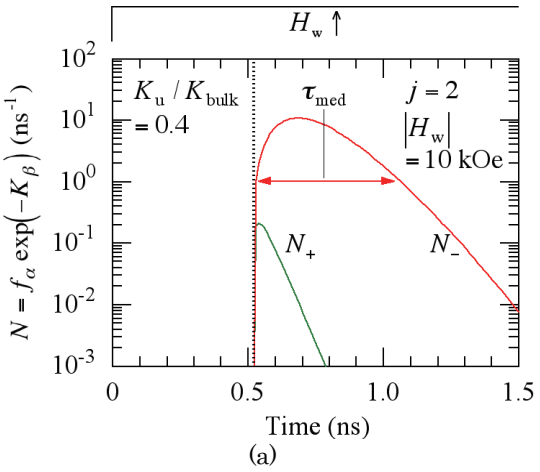

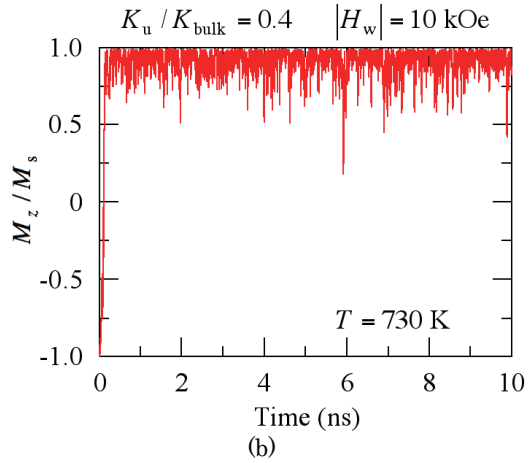

Fig. 18 (a) Mean magnetization reversal number per unit time $N = f_\alpha \exp(-K_\beta)$ as a function of time where N_- = 10.7 ns^{-1} and N_+ = 0.01 ns^{-1} at 0.68 ns (730 K) and (b) time dependence of magnetization z component M_z/M_s at 730 K (0.68 ns) where K_u/K_{bulk} = 0.4, $|H_w|$ = 10 kOe, and H_{keff} = 30 kOe.

where the calculation step time Δt was 0.2 ps.

The relationships between the bER and SNR values are shown in Fig. 15. We observe a good correlation between them.

The $|H_w|$ value dependences of the 2 grain bER value for column numbers j of 1 to 4 are shown in Fig. 16 for K_u/K_{bulk} = 0.4.

The bER value for j = 1 in Fig. 16 where K_u/K_{bulk} = 0.4 is small compared with that for j = 1 in Fig. 3 (b) where K_u/K_{bulk} = 0.8. The reasons for this are as follows. Figure 17 shows the N_- value as a function of time during writing for K_u/K_{bulk} = 0.4, j = 1, and $|H_w|$ = 10 kOe. The τ_{med} value in Fig. 17 is long compared with that in Fig. 4. Since the τ_{med} value is long, the probability increases that the magnetization reverses into the recording field direction even if there is EBW. Since the N_- value is sufficiently small at the end of the field writing time of 2.07 ns, the bER caused by EAW is negligible.

On the other hand, the bER value for j = 2 in Fig. 16 (K_u/K_{bulk} = 0.4) is smaller than that for j = 2 in Fig. 3

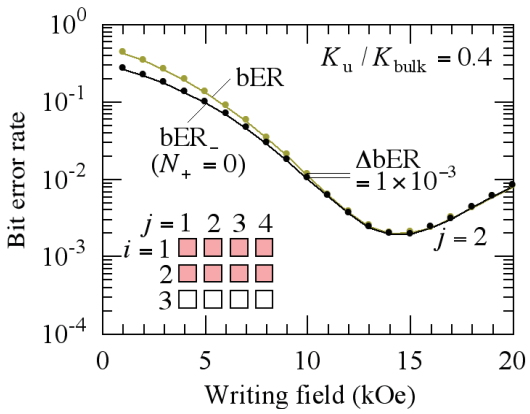

Fig. 19 Comparison of two cases of writing field $|H_w|$ dependence of 2 grain bER for column number $j = 2$ where $K_u/K_{bulk} = 0.4$. The bER value was calculated using both N_- and N_+, and the bER_ value was calculated using only N_- where $N_+ = 0$.

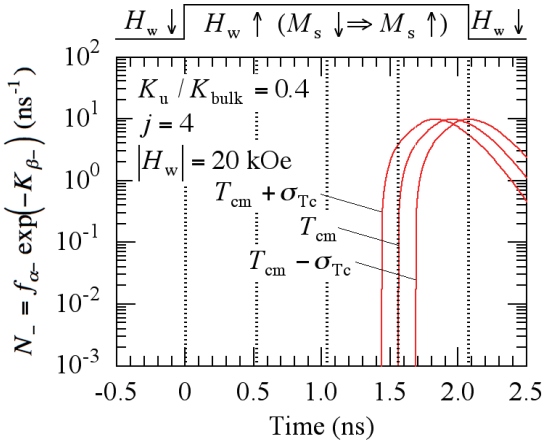

Fig. 20 Mean magnetization reversal number per unit time $N_- = f_{\alpha-} \exp(-K_{\beta-})$ as a function of time during writing for Curie temperatures of $T_{cm} + \sigma_{Tc}$, T_{cm}, and $T_{cm} - \sigma_{Tc}$ where $K_u/K_{bulk} = 0.4$, $j = 4$, and $|H_w| = 20$ kOe.

(b) ($K_u/K_{bulk} = 0.8$) when the $|H_w|$ value is small, and the bER value in Fig. 16 is larger when the $|H_w|$ value is large. The N_- value is small at the end of the field writing time of 2.07 ns at 10 kOe. However, the N_- value becomes large at 20 kOe. Therefore, EAW is large when the $|H_w|$ value is large.

When $K_u/K_{bulk} = 0.4$ and $|H_w| = 10$ kOe, the N_- value for $j = 2$ exhibits its maximum value at 0.68 ns, which corresponds to a temperature of 730 K, as shown in Fig. 18 (a). The $1/N_-$ value was 0.093 ns at 730 K and the τ_{med} value increased to 0.55 ns compared with $1/N_- = 0.073$ ns and $\tau_{med} = 0.25$ ns for $K_u/K_{bulk} = 0.8$ and $|H_w| = 10$ kOe as shown in Fig. 10 (a). Therefore, WE decreases due to the longer τ_{med}. Figure 18 (b) shows the time dependence of M_z/M_s at 730 K where $|H_w| = 10$ kOe and $H_{keff} = 30$ kOe. Since $N_+ = 0.01$ ns^{-1} at 730 K, only 0.1 mean magnetization reversals occur within 10 ns in the $-z$ direction. Therefore, it can be seen that there is no magnetization motion in the $-z$ direction for the example shown in Fig. 18 (b).

Figure 19 shows the bER value calculated using both N_- and N_+, and the bER_ value calculated using only N_- where $N_+ = 0$. The difference between the results in Figs. 12 and 19 can be explained in terms of the difference between the results in Figs. 10 (a) and 18 (a). The bER_ values are 4.8×10^{-2} for $K_u/K_{bulk} = 0.8$ and 1.0×10^{-2} for 0.4 at $|H_w| = 10$ kOe as shown in Figs. 12 and 19, since the τ_{med} values are 0.25 and 0.55 ns as shown in Figs. 10 (a) and 18 (a), respectively. The ΔbER values are 8×10^{-3} for $K_u/K_{bulk} = 0.8$ and 1×10^{-3} for 0.4 at $|H_w| = 10$ kOe as shown in Figs. 12 and 19, since the maximum value of N_+ for $K_u/K_{bulk} = 0.8$ is larger than that for 0.4 as shown in Figs. 10 (a) and 18 (a), respectively.

When compared with the bER values for $j = 4$ in Figs. 3 (b) and 16, the bER value for the medium with $K_u/K_{bulk} = 0.4$ is rather large, since the N_- value is very large at the end of the field writing time of 2.07 ns as shown in Fig. 20.

As the K_u/K_{bulk} value decreases, the bER value becomes smaller when the $|H_w|$ value is small, and it becomes larger when the $|H_w|$ value is large as shown in Fig. 14 (a). When using a small K_u/K_{bulk} medium, the h value must be increased, taking account of 10 years of archiving and ATI for practical use. Nevertheless, reducing K_u/K_{bulk} may improve the bER value even in HAMR. However, since the influence of EAW is large in HAMR, we may not reduce the K_u/K_{bulk} value to 0.4 in HAMR as is possible in HDMR[4,5].

4. Conclusions

We analyzed the error factors for writability in HAMR in terms of erasure-before-write (EBW), erasure-after-write (EAW), Curie temperature T_c variation, write-error (WE), statistical factor, and anisotropy constant K_u with a constant grain height.

One cause of EBW is T_c variation. However, EBW may also occur in granular media with no T_c variation, since the grain position fluctuates. And T_c variation makes EAW large.

An increase in grain number per bit is advantageous for reducing the bit error rate in terms of the statistical factor. However, that is disadvantageous as regards manufacturability.

HAMR with a small K_u is advantageous for EBW and disadvantageous for EAW because of the long medium writing time τ_{med}.

HAMR with a small K_u has an advantage for WE thanks to the long τ_{med} value and small magnetization reversal number per unit time N_+ in the opposite direction to the recording direction.

Acknowledgement We acknowledge the support of the Advanced Storage Research Consortium (ASRC), Japan.

References

1) S. H. Charap, P. -L. Lu, and Y. He: *IEEE Trans. Magn.*, **33**,

978 (1997).
2) J. -G. Zhu and H. Li: *IEEE. Trans. Magn.*, **49**, 765 (2013).
3) H. Li and J. -G. Zhu: *J. Appl. Phys.*, **115**, 17B744 (2014).
4) F. Akagi, M. Mukoh, M. Mochizuki, J. Ushiyama, T. Matsumoto, and H. Miyamoto: *J. Magn. Magn. Mater.*, **324**, 309 (2012).
5) T. Kobayashi, Y. Nakatani, and I. Tagawa: *J. Magn. Soc. Jpn.*, **48**, 81 (2024).
6) M. Mansuripur and M. F. Ruane: *IEEE Trans. Magn.*, **MAG-22**, 33 (1986).
7) J. -U. Thiele, K. R. Coffey, M. F. Toney, J. A. Hedstrom, and A. J. Kellock: *J. Appl. Phys.*, **91**, 6595 (2002).
8) T. Kobayashi, Y. Nakatani, and Y. Fujiwara: *J. Magn. Soc. Jpn.*, **47**, 1 (2023).
9) E. D. Boerner and H. N. Bertram: *IEEE Trans. Magn.*, **34**, 1678 (1998).
10) T. Kobayashi and I. Tagawa: *J. Magn. Soc. Jpn.*, **47**, 128 (2023).
11) T. Kobayashi, Y. Nakatani, and Y. Fujiwara: *J. Magn. Soc. Jpn.*, **42**, 110 (2018).
12) Fujitsu Release: *New Version of EXAMAG LLG Simulator*, https://www.fujitsu.com/global/about/resources/news/press-releases/2015/0324-01.html (2015).
13) T. Kobayashi, I. Tagawa, and Y. Nakatani: *J. Magn. Soc. Jpn.*, **49**, 1 (2025).

Received Jan. 12, 2025; Accepted May 13, 2025

J. Magn. Soc. Jpn., **49**, 58-61 (2025) <Letter>

Atomistic Spin Simulation of Néel Vector Rotation by Spin-Orbit Torque in Spin-Flopped Ferrimagnetic Thin Films

T. Mandokoro*, Y. Shiota*,**, I. Sugiura*, R. Hisatomi*,**, S. Karube*,**, and T. Ono*,**
* Institute for Chemical Research (ICR), Kyoto Univ., *Gokasho, Uji, Kyoto 611-0011, Japan*
** Center for Spintronics Research Network (CSRN), Kyoto Univ., *Gokasho, Uji, Kyoto 611-0011, Japan*

Spin superfluidity is a phenomenon suitable for long range transport of spin angular momentum and requires rotation of the Néel vector within magnetic easy-plane. Recently, we demonstrated Néel vector rotation induced by spin-orbit torque in a spin-flopped ferrimagnet, which can be regarded as an ideal easy-plane antiferromagnet. However, the detailed dynamics of the Néel vector with respect to material parameters have remained unclear. In this paper, we investigate the effect of damping constant, magnetic anisotropy, current density, thickness and spin diffusion length on Néel vector rotation using atomistic spin simulation. While magnetic anisotropy can be disregarded for current densities well above the threshold, its influence becomes significant near the threshold current density. These results provide important insights into Néel vector rotation and spin superfluidity.

Keywords: Néel vector, spin dynamics, ferrimagnet, spin-orbit torque, atomistic spin simulation

1. Introduction

Spintronics have garnered considerable attention as a novel technological foundation that surpasses conventional electronics by harnessing not only the charge but also the spin of electrons[1,2]. Unlike charge currents, pure spin currents carry no net charge and thus generate no Joule heating, avoiding thermal energy losses. Therefore, spin currents are considered as a highly efficient means of information transfer and expected to play an important role in low-power next generation devices [3-5].

Spin transport can be mediated by spin waves or by a more exotic mechanism known as spin superfluidity [6-11]. They exhibit markedly different transport characteristics. Spin wave exhibits exponential attenuation with distance, limiting their potential for long-range transport. In contrast, spin superfluidity enables extended spin transport due to its linear attenuation. In this phenomenon, spin angular momentum is transmitted through the rotation of magnetization within the magnetic easy-plane [7-11].

In ferromagnets, long-range dipolar interactions affect spin superfluid transport, limiting its propagation over long distance. Therefore, antiferromagnets are an ideal platform for spin superfluidity [9-11]. To realize the spin superfluidity in antiferromagnets, the Néel vector rotation within the magnetic easy-plane is required. Its excitation has been examined in several theoretical and experimental studies on both collinear and non-collinear antiferromagnets [12-15]. Recently, we have demonstrated the Néel vector rotation by spin-orbit torque (SOT) in the spin-flop phase of amorphous ferrimagnets [16]. The use of

Table 1 Parameters used in simulations

Parameter	Value (Co/Gd)
Atomic composition [%]	72/28 [16]
Spin diffusion length λ [nm]	5 [19]
Intra-lattice exchange energy [J/m^3]	$4.28\times10^7/1.08\times10^6$ [20]
Inter-lattice exchange energy [J/m^3]	-9.25×10^6 [21]
Magnetic moment [μ_B]	1.85/4.85 [16]
Gyromagnetic ratio γ [rad Hz/T]	$1.86\times10^{11}/1.78\times10^{11}$ [21]
Gilbert damping constant α	0.01-0.10 [20,22,23]
Effective spin Hall angle θ_{SH}	0.21/0.03 [24]

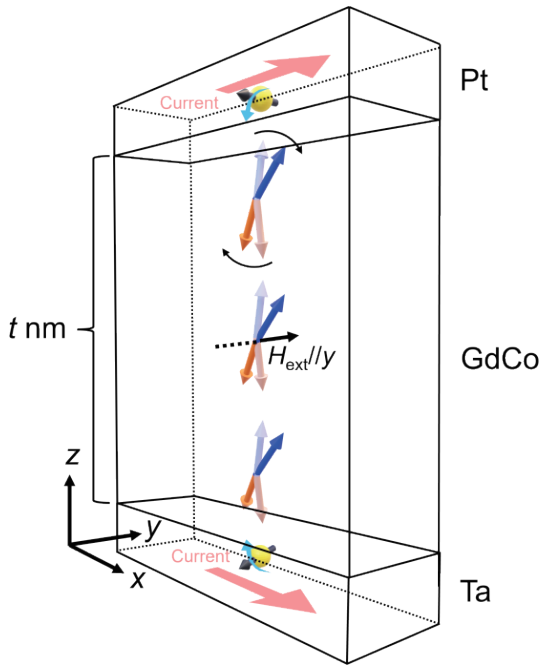

Fig. 1 Schematic illustration of simulation setup.

Corresponding author: T. Ono (e-mail: ono@scl.kyoto-u.ac.jp).

spin-flopped ferrimagnets allows the design of systems with tailored magnetic properties – such as magnetic anisotropy, damping, and composition – offering greater experimental flexibility than intrinsic easy-plane antiferromagnets, which are limited in materials choice. The detailed dynamics of the Néel vector rotation with respect to the material parameters, such as damping constant, magnetic anisotropy, film thickness, and spin diffusion length, remain unclear while there have been several studies.

In this paper, we investigated the time evolution of spin dynamics associated with the Néel vector rotation induced by SOT in ferrimagnetic thin films under various conditions using the atomistic spin simulation "VAMPIRE" [15,16]. In contrast to macroscopic simulations, atomic simulations incorporate spin diffusion length and describe systems in which two magnetic atoms are randomly arranged, such as amorphous materials. Accordingly, we employed the atomistic spin-dynamics package "VAMPIRE" to construct a realistic model of the system under investigation. It was found that magnetic anisotropy causes the Néel vector rotation to deviate from a sinusoidal behavior near the threshold current density. As the current density increases, the influence of magnetic anisotropy becomes negligible, and the rotation frequency approaches that observed in the system without magnetic anisotropy. Furthermore, the rotation frequency decreases monotonically with increasing thickness.

2. Setup and parameters

Based on the experimentally demonstrated system we have previously reported [16], we consider a Ta / GdCo (t: 3 – 19 nm) / Pt trilayer structure, as shown in Fig. 1. The two heavy metal layers with different signs of spin Hall angles are attached to the top and bottom of the magnetic layer to efficiently excite the Néel vector rotation. In the simulation setup, the spin current was injected into the GdCo layer from the top and bottom layers in an equal ratio. The in-plane direction of the unit cell was modeled under periodic boundary conditions. Due to the limitations of the simulation program, the thin film was divided into 49 segments along the thickness direction.

The parameters used in simulations are summarized in Table 1. The atomic composition and magnetic moment of each Co and Gd sublattice were taken from the previous experimental values at 240 K [14]. Other parameters were taken from the literature [19-24]. For simplicity, the spin torque was assumed to be only damping-like torque, and the thermal fluctuations were neglected by setting the temperature to 0 K.

The Néel vector rotation requires the magnetic easy-plane. However, amorphous ferrimagnets such as GdCo alloy inherently lack magnetic easy-planes due to the absence of crystalline structure. To overcome this limitation, we utilize a pseudo-magnetic easy-planes induced by a spin-flop transition under an external magnetic field. First, the system was initialized with randomly oriented atomic magnetic moments and then relaxed under an external magnetic field ($H_{\mathrm{ext}}//y$) of 8 T, where the occurrence of spin-flop was confirmed. Simultaneously, an electric current was applied to the system to induce SOT, enabling the computation of the Néel vector dynamics. Finally, the rotation frequencies and the dynamics of the Néel vector were evaluated for various situations.

3. Atomistic simulation and discussion

3.1 Dependence of damping constant

Previous theoretical studies have shown that the frequency of the Néel vector rotation in biaxial antiferromagnet is inversely proportional to the damping constant α [25,26]. However, in the case of spin-flopped ferrimagnets, it is not obvious whether the frequency depends on $1/\alpha$, therefore we investigated the dependence of the damping constant on the rotation frequency.

The green dots in Fig. 2 show the dependence of the damping constant on the calculated rotation frequency for a thickness $t = 3$ nm without magnetic anisotropy under the current density of 7.69×10^{11} A/m^2. In this case, the rotation frequency exhibited an inverse proportionality to the damping constant, which is in accordance with theoretical prediction. Then, to investigate the effect of the uniaxial magnetic anisotropy along perpendicular to the film plane K_{u}, we also performed calculations including a uniaxial magnetic anisotropy of 6.01×10^3 J/m^3, which was experimentally obtained in previous study [16], as shown in red dots in Fig. 2. In this case, the rotation frequency deviates from the ideal $1/\alpha$ behavior. This is because the applied current density of 7.69×10^{11} A/m^2 slightly exceeds the threshold current density, and the Néel vector rotation

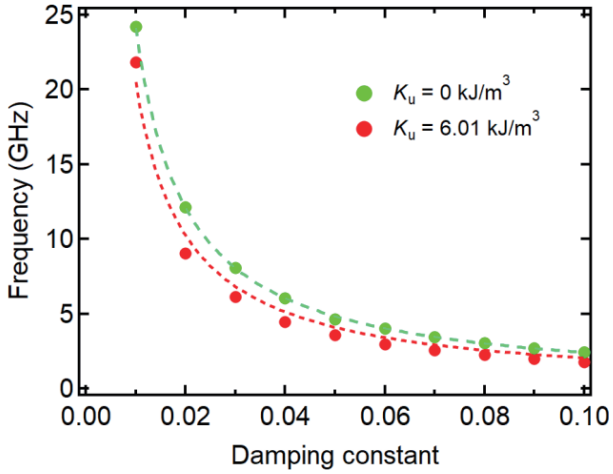

Fig. 2 Dependences of rotation frequency on damping constant. Green and red dots represent calculation results for cases without and with magnetic anisotropy, respectively. Red and green dotted lines represent $1/\alpha$ fitting for each case.

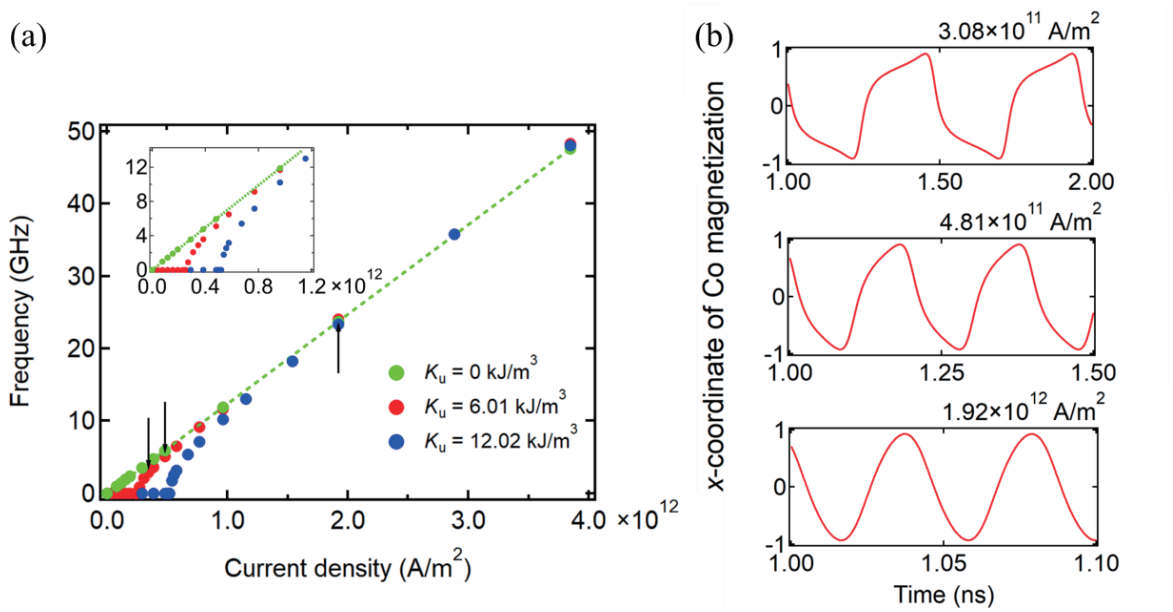

Fig. 3 (a) Dependence of rotation frequency on current density. Green, red, and blue dots represent calculation results for $K_u = 0\ \mathrm{J/m^3}$, $6.01 \times 10^3\ \mathrm{J/m^3}$, and $12.02 \times 10^3\ \mathrm{J/m^3}$, respectively. Green dotted line is a linear fit for case of $K_u = 0\ \mathrm{J/m^3}$. Inset shows an enlarged view at small current density. (b) Three lines show dynamics of Co magnetization at several current densities for case of $K_u = 6.01 \times 10^3\ \mathrm{J/m^3}$ indicated by black arrows in Fig. 3 (a).

deviates from the sinusoidal behavior, as will be discussed in Section 3.2.

3.2 Dependence of current density

To investigate the effect of the uniaxial magnetic anisotropy on the rotational dynamics of the Néel vector, we calculated the current density dependence of the rotation frequency while fixing the damping constant α at 0.05. Figure 3 (a) shows the results for the systems with and without uniaxial magnetic anisotropy. In the absence of K_u (green dots), no threshold behavior is observed, and the rotation frequency increases linearly with current density (green dotted line). On the other hand, when K_u is finite (red and blue dots), a threshold current density for the excitation of the Néel vector rotation appears, and the frequency rotation deviates from linearity near the threshold current density. This nonlinearity is further corroborated by the distortion of the magnetization dynamics from ideal sinusoidal behavior as the current density approaches the threshold, as shown in Fig. 3 (b). We also notice that the threshold current density increases with increasing the magnetic anisotropy, approximately doubling when K_u is doubled. From the above, it can be considered that magnetic anisotropy has a significant effect only near the threshold current density.

3.3 Dependence of thickness

Thus far, our investigation has focused on the dynamics of the Néel vector rotation in $t = 3\ \mathrm{nm}$, corresponding to the experimental conditions used in our previous study [16]. As the thickness of the magnetic layer increases, the total spin angular momentum increases. Therefore, the rotational frequency is expected to be suppressed because the applied energy density per spin angular momentum decreases. In the following, we examine the dependence of the rotation frequency on the film thickness and spin diffusion length to verify this expectation.

Figure 4 shows the thickness dependence of the rotation frequency for the system without and with uniaxial magnetic anisotropy under the current density of $7.69 \times 10^{11}\ \mathrm{A/m^2}$. The rotation frequency decreases with increasing film thickness because the injected spin current per unit volume decreases. It is noteworthy that in the case of the system with $K_u = 6.01 \times 10^3\ \mathrm{J/m^3}$ (red dots), the total magnetic anisotropy energy of the entire system increases with thickness, resulting in more pronounced decrease in rotation frequency compared to $K_u = 0\ \mathrm{J/m^3}$(green dots). This can be explained as follows. In systems with uniaxial magnetic anisotropy, the total magnetic anisotropy energy increases with increasing

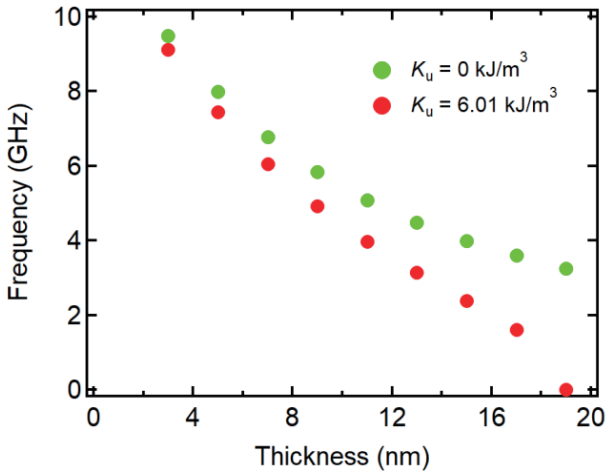

Fig. 4 Dependence of rotation frequency on thickness. Green and red dots represent calculation results for cases of $K_u = 0\ \mathrm{J/m^3}$ and $K_u = 6.01 \times 10^3\ \mathrm{J/m^3}$.

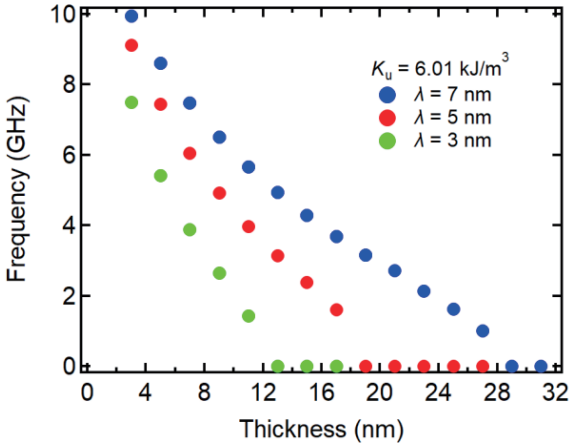

Fig. 5 Dependence of rotation frequency on thickness for several spin diffusion lengths λ. Blue, red and green dots represent calculation results for cases of $\lambda = 7, 5, 3$ nm, respectively.

film thickness. As a result, the threshold current density also increases and approaches the applied current density, leading to a decrease in the rotation frequency. In the system with uniaxial magnetic anisotropy at $t = 19$ nm, the threshold current density exceeds the applied one, and thus the Néel vector rotation is no longer excited.

Figure 5 shows the thickness dependence of the rotation frequency for several spin diffusion lengths. The rotation frequency decreases monotonically as the spin diffusion length is reduced. This behavior is attributed to the reduced volume fraction over which the injected spin current can exert torque, resulting in a dilution of the effective torque density.

4. Conclusion

In this study, we investigated the effects of the damping constant, magnetic anisotropy, the current density, thickness and spin diffusion length on the Néel vector rotation. When a current large enough to overcome magnetic anisotropy is applied, magnetic anisotropy can be negligible in the Néel vector rotation. Magnetic anisotropy affects dynamics near the threshold current, causing it to deviate from the sinusoidal curve behavior. Furthermore, the rotation frequency decreases monotonically with increasing thickness. The rotation frequency also decreases with decreasing spin diffusion length. The results obtained in this study provide important insights into the Néel vector rotation and spin superfluidity.

Acknowledgements This work was partially supported by JSPS KAKENHI (JP20H05665, JP21K18145, JP24H00007, JP22H01936, JP24H02233), MEXT Initiative to Establish Next-generation Novel Integrated Circuits Centers (X-NICS) Grant Number JPJ011438, and Collaborative Research Program of the Institute for Chemical Research, Kyoto University.

References

1) A. Hirohata, K. Yamada, Y. Nakatani, L. Prejbeanu, B. Diény, P. Pirro, and B. Hillebrands: *J. Magn. Magn. Mater.*, **509**, 166711 (2020).
2) Y. Guo, X. Zhang, Z. Huang, J. Chen, Z. Luo, J. Zhang, J. Li, Z. Zhang, J. Zhao, X. Han, and H. Wu: *npj Spintronics*, **2**, 36 (2024).
3) T. Schneider, A. A. Serga, B. Leven, B. Hillebrands, R. L. Stamps, and M. P. Kostylev: *Appl. Phys. Lett.*, **92**, 022505 (2008).
4) Y. Kajiwara, K. Harii, S. Takahashi, J. Ohe, K. Uchida, M. Mizuguchi, H. Umezawa, H. Kawai, K. Ando, K. Takanashi, S. Maekawa, and E. Saitoh: *Nature*, **464**, 262 (2010).
5) H. Wang, R. Yuan, Y. Zhou, Y Zhang, J. Chen, S. Liu, H. Jia, D. Yu, J. P. Ansermet, C. Song, and H. Yu: *Phys. Rev. Lett.*, **130**, 096701 (2023).
6) B. I. Halperin and P. C. Hohenberg: *Phys. Rev.*, **188**, 898 (1969).
7) E. B. Sonin: *Adv. Phys.*, **59**, 181 (2010).
8) H. Skarsvåg, C. Holmqvist, and A. Brataas: *Phys. Rev. Lett.*, **115**, 237201 (2015).
9) S. Takei, B. I. Halperin, A. Yacoby, and Y. Tserkovnyak: *Phys. Rev. B*, **90**, 094408 (2014).
10) E. B. Sonin: *Phys. Rev. B*, **95**, 144432 (2017).
11) A. Qaiumzadeh, H. Skarsvåg, C. Holmqvist, and A. Brataas: *Phys. Rev. Lett.*, **118**, 137201 (2017).
12) Y. Takeuchi, Y. Yamane, J. Y. Yoon, R. Itoh, B. Jinnai, S. Kanai, J. Ieda, S. Fukami, and H. Ohno: *Nat. Mater.* **20**, 1364 (2021).
13) S. Sakamoto, T. Nomoto, T. Higo, Y. Hibino, T. Yamamoto, S. Tamaru, Y. Kotani, H. Kosaki, M. Shiga, D. N. Hamane, T. Nakamura, T. Nozaki, K. Yakushiji, R. Arita, S. Nakatsuji and S. Miwa: *Nat. Nanotechnol.* **20**, 216 (2025).
14) V. Puliafito, R. Khymyn, M. Carpentieri, B. Azzerboni, V. Tiberkevich, A. Slavin, and G. Finocchio: *Phys. Rev. B*, **99**, 024405 (2019).
15) A. Shukla, S. Qian, and S. Rakheja: *APL. Mater.*, **11**, 091110 (2023).
16) T. Mandokoro, Y. Shiota, T. Ito, H. Matsumoto, H. Narita, R. Hisatomi, S. Karube, and T. Ono: *arXiv*:2503.08882 (2025).
17) R. F. L. Evans, W. J. Fan, P. Chureemart, T. A. Ostler, M. O. A. Ellis, and R. W. Chantrell: *J. Phys.: Condens. Matter*, **26**, 103202 (2014).
18) T. A. Ostler, R. F. L. Evans, and R. W. Chantrell, U. Atxitia, O. C. Fesenko, I. Radu, R. Abrudan, F. Radu, A. Tsukamoto, A. Itoh, A. Kirilyuk, T. Rasing, and A. Kimel: *Phys. Rev. B*, **84**, 024407 (2011).
19) Y. Lim, B. Khodadadi, J. F. Li, D. Viehland, A. Manchon, and S. Emori: *Phys. Rev. B*, **103**, 024443 (2021).
20) D. H. Suzuki, B. H. Lee, and G. S. D. Beach: *Appl. Phys. Lett.*, **123**, 122401 (2023).
21) B. I. Min and Y. R. Jang: *J. Phys.: Condens. Matter*, **3,** 5131 (1991).
22) T. Okuno, S. K. Kim, T. Moriyama, D. H. Kim, H. Mizuno, T. Ikebuchi, Y. Hirata, H. Yoshikawa, A. Tsukamoto, K. J. Kim, Y. Shiota, K. J. Lee, and T. Ono: *Appl. Phy. Express*, **12**, 093001 (2019).
23) S. Funada, T. Nishimura, Y. Shiota, S. Kasukawa, M. Ishibashi, T. Moriyama, and T. Ono: *Jpn. J. Appl. Phys.*, **58**, 080909 (2019).
24) G. Sala, C. H. Lambert, S. Finizio, V. Raposo, V. Krizakova, G. Krishnaswamy, M. Weigand, J. Raabe, M. D. Rossell, E. Martinez, and P. Gambardella: *Nat. Mater.*, **21**, 640 (2022).
25) S.Takei, B. I. Halperin, A. Yacoby, and Y. Tserkovnyak: *Phys. Rev. B*, **90**, 094408 (2014).
26) A. Qaiumzadeh, H. Skarsvåg, C. Holmqvist, and A. Brataas: *Phys. Rev. Lett.*, **118**, 137201 (2017).

Received May 12, 2025; Revised May 26, 2025; Accepted Jun. 02, 2025

Editorial Committee Members・Paper Committee Members

Notice for Photocopying

編集委員・論文委員

複写をされる方へ

Journal of the Magnetics Society of Japan

Vol. 49 No. 4 (通巻第399号) 2025年7月1日発行

Vol. 49 No. 4 Published Jul. 1, 2025
by the Magnetics Society of Japan
Tokyo YWCA building Rm207, 1–8–11 Kanda surugadai, Chiyoda-ku, Tokyo 101–0062
Tel. +81–3–5281–0106 Fax. +81–3–5281–0107

Printed by JPC Co., Ltd.
Sports Plaza building 401, 2–4–3, Shinkamata Ota-ku, Tokyo 144–0054
Advertising agency: Kagaku Gijutsu-sha

発行：(公社)日本磁気学会 101–0062 東京都千代田区神田駿河台 1–8–11 東京YWCA会館 207 号室
製作：ジェイピーシー 144–0054 東京都大田区新蒲田 2–4–3 スポーツプラザビル401 Tel.（03）6715–7915
広告取扱い：科学技術社 111–0052 東京都台東区柳橋 2–10–8 武田ビル 4F Tel.（03）5809–1132